Research Article

Structural, electrical and dielectric characteristics of strontium-modified $CaCu_3Ti_4O_{12}$

Madhusmita Sahu[1] · Sugato Hajra[2] · R. N. P. Choudhary[1]

Abstract

In order to produce an ultra-high dielectric constant and low loss factor in a polycrystalline material of Sr^{+2}-modified (concentration 15%) $CaCu_3Ti_4O_{12}$ (i.e., $Ca_{0.85}Sr_{0.15}Cu_3Ti_4O_{12}$, abbreviated as CSCTO-15) was prepared using a cost-effective solid-state reaction technique. Structural analysis using Rietveld refinement of the X-ray diffraction data has confirmed that the sample crystallizes in a cubic system with space group symmetry of Im3. Morphological/microstructural analysis of the natural surface of a pellet shows dense grain growth, with clearly visible grain boundaries. The dielectric relaxation mechanism of CSCTO-15 has been revealed by the detailed study of frequency- and temperature-dependent dielectric parameters (ε_r and tan δ). Analysis of the frequency and temperature dependence of impedance and related parameters, collected by a complex impedance spectroscopic technique, has provided and estimated the contributions of grain, grain boundaries and electrode in the electrical process in the material. The activation energy at high temperatures has been calculated from the temperature-dependent ac conductivity plots at selected frequencies.

Keywords Structural · Impedance · Electrical properties · Dielectric

1 Introduction

Over the past several years, certain perovskite (simple or complex) materials of a general chemical formula ABO_3 (A = mono-divalent, B = tri to hexavalent ions) having giant dielectric permittivity ($\epsilon_r \approx 10^5$) have been found useful in the field of microelectronics for the fabrication of devices including spintronics and energy storage devices [21]. Subramanian et al. first reported a giant dielectric constant (~ 10^4) in $CaCu_3Ti_4O_{12}$ (CCTO) over a wide temperature and frequency range [24]. Since then, extensive studies have been performed to tailor the dielectric properties (i.e., enhancement of dielectric constant and decrease the tangent loss factor) of CCTO by suitable substitution at its different atomic sites and/or fabrication of solid solution/composites with other perovskites. In this process, modification of CCTO with a Ca-site of a general chemical composition $ACu_3Ti_4O_{12}$ (A = $Na_{1/2}Y_{1/2}$, $Y_{2/3}$, $Bi_{2/3}$) and other related materials exhibits enormously high dielectric permittivity (ϵ_r) with weak frequency and temperature dependence over a wide range [5]. In order to understand the origin of the giant dielectric constant and low loss factor of CCTO, several models or mechanisms have been proposed, including local dipole moments associated with off-center displacement of Ti ions [20], multi-layer capacitance (MLC) [14], nano-barrier layer capacitor (NBLC) [35], nanoscale disorder (NSD), surface barrier layer capacitor (SBLC), and internal domain [8, 19] models. Amongst all the models, the internal barrier layer capacitor (IBLC) model has been found to be the most acceptable mechanism and/or explanation for the high dielectric constant of CCTO. According to the IBLC model, CCTO behaves as an electrically heterogeneous ceramic containing insulating grain boundaries (GBs) and semiconducting grains (Gs), as

✉ Madhusmita Sahu, mssahu1592@gmail.com | [1]Department of Physics, Multifunctional and Advance Materials Laboratory, Siksha 'O' Anusandhan (Deemed to be University), Bhubaneswar, Odisha 751030, India. [2]Department of Electronics and Instrumentation, Siksha 'O' Anusandhan (Deemed to be University), Bhubaneswar, Odisha 751030, India.

reported by Adams et al. [1] and Zhang et al. [36]. Hence, if we can alter the electrical properties of GBs and Gs, we can induce good dielectric properties ($\in_r$ and tanδ) in the material.

Generally, dielectric properties are strongly dependent on various factors, which include the concentration of doped ions into the parent compound, sintering conditions and microstructure. Recent works have reported on doping the suitable ions at the Ca, Cu and/or Ti sites of CCTO to enhance the dielectric properties [2, 30]. The Ca and Cu disorder in CCTO (at nanometer scale) was analyzed using superior quantitative electron diffraction (QED) and extended X-ray absorption fine structure (EXAFS) analysis. The increased permittivity was proposed to be a result of the modified electronic structure of the defect Cu cation on the A site [29]. The relaxation and conduction mechanism using dielectric and modulus spectroscopy of 15 wt% of Sr in CCTO was not extensively reported as discerned from the vast literature. Similar composition was reported by Vangchangyia et al. [31], showing a dielectric constant of 11432 and loss tangent of 0.025 at 20 °C and 1 kHz. Among the Sr-CCTO specimens reported by Xue et al. [33], Sr-CCTO-2, with Sr doping concentration of 10%, exhibited the highest permittivity and the lowest nonlinear coefficient. In a study by Li et al. [15] the dielectric properties demonstrated that, with dopant weight % ≤ 0.15, Sr doping in CCTO not only increased dielectric permittivity but also reduced dielectric loss; however, it also reduced the dependence on frequency at low frequencies. In addition, we have taken different particle size of starting ingredients for the preparation of CSCTO-15.

In the present communication, we primarily report the basic crystal data, morphology, and dielectric and impedance characteristics of strontium-modified $CaCu_3Ti_4O_{12}$, (i.e., $Ca_{0.85}Sr_{0.15}Cu_3Ti_4O_{12}$), fabricated with nano-sized powders of CuO (< 50 nm, particle size) and TiO_2 (21 nm, particle size) and micro-sized powders of $CaCO_3$ and $SrCO_3$, which is the main motivation behind this attempt.

2 Experimental details

High-purity (> 99.99%) starting materials of different particle sizes, including $SrCO_3$ (M/s Sigma Aldrich), $CaCO_3$, (M/s Sigma Aldrich), CuO (< 50 nm) and TiO_2 (21 nm) (M/S Sigma Aldrich), in required stoichiometric amounts, were used for the fabrication of polycrystalline samples of CSCTO-15. Fine powders of the materials were mixed in dry and wet medium for 2 h with the help of a pestle and an agate mortar. The mixed powder was set aside in a high-purity alumina crucible and heated in a muffle furnace at 600 °C for 4 h. Preferably, the kinetics of the quick conventional solid-state reaction at a microscopic level at high temperature

is promoted with the use of TiO_2 and CuO_2 nano-sized powders at the start of sample preparation with micron-sized $CaCO_3$ and $SrCO_3$ powders. The room-temperature X-ray powder diffraction (XRD) data were obtained using a high-resolution Bruker D8 diffractometer for structural characterization of CSCTO-15. Cylindrical pellets of 12 mm in diameter and 1.8 mm thick were then prepared from the calcined powder at a pressure of 4×10^7 N/m² with the help a uniaxial hydraulic press. After making a pellet, it was sintered at 1200 °C for 12 h (total programming time) and furnace-cooled to room temperature. The presence of a minor peak of TiO_2 in a pure CCTO sample with sintering at 1200 °C for 8 h was also reported by Hu et al. [10]; thus this sintering temperature was preferred. However, thermogravimetric and dilatometry testing could provide more relevant information about the calcination and sintering temperature, but this was not possible due to limitation of instruments. Scanning electron microscopy (Zeiss EVO-18) was utilized to explore the microstructure of the CSCTO-15 pellet and pure CCTO. Then, both surfaces of the disc-shaped pellet were made even as well as parallel. The (sintered) pellet was coated with a thin layer of silver paste to create an electrode, followed by heat treatment at 250 °C for about 1 h in order to make it moisture free and further characterize its impedance and dielectric properties. The electrical parameters (dielectric constant, dissipation factors, impedance data, etc.) were recorded using a computer-controlled LCR meter (M/S PSM 1735, N4L) over a broad frequency range (1 kHz to 2 MHz) at different temperatures (25–315 °C).

3 Results and discussion

3.1 Structural and microstructural analysis

The room-temperature XRD pattern of CCTO and the sintered specimen (CSCTO-15) showed highly crystalline behavior (Fig. 1a, b). Rietveld structural analysis of the sample was carried out for the refinement of crystal data using the XRD pattern. The phase of the parent compound (CCTO) has been identified with some major peaks including (220), (400) and (422) peaks, which obey the extinction rule of the reported space group (i.e., for $h\,k\,l$ reflection $h + k + l = 2n$, for $h\,h\,l$: reflection $l = 2n$, for $h\,0\,0$ reflections $h = 2n$, for $0\,k\,l$ reflections $k + l = 2n$" [25]. A few small-intensity impurity peaks are also observed. The sharp peaks confirm that the synthesized compound (CSCTO-15) is highly crystalline in nature. The reliability and correctness of the structural refinement were demonstrated using index parameters including weighted residual error (R_w), Bragg factor (R_b), expected factor (R_{exp}), and goodness of fit expressed by the Rw/R_{exp} ratio. The
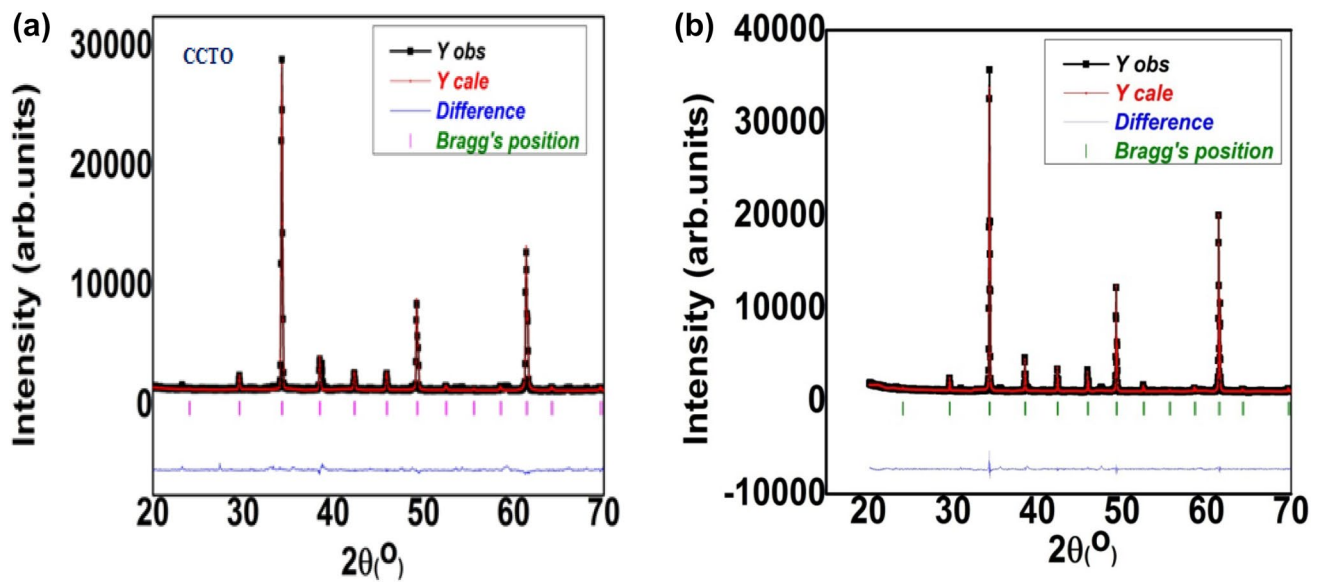
Fig. 1 Structural refinement of sintered **a** CCTO and **b** CSCTO-15 samples

software used for Rietveld refinement is POWD MULT. The JCPDS card number 75-2188 is used to refine the structure. Table 1 shows the reliability parameters of pure CCTO and 15 wt% Sr-doped CCTO. This suggests the best-quality fitting of the experimental data with the theoretical data. The little high *R*-factors may originate by a little high of noise at the background of the XRD spectra, as described by Jansen et al. [12].

The grains and grain boundaries of pure CCTO were observed from micrographs to have high densification [25]. Figure 2a, b shows the SEM micrographs of the CCTO and CSCTO-15 sintered pellet. The figure clearly shows the distinct grains of almost equal dimensions. Interlinking between grains (boundary) is also clearly visible. The size of some grains for CSCTO-15 was calculated using ImageJ image analysis software. Due to the influence of chemical homogenization, the microstructure of the product and very clear grain boundaries are depicted. The grain morphology indicates that said compound is fully dense. During the sintering stage, these are intimately connected with the presence of the liquid phase of (CuO) and oxygen vacancy at grains and grain boundaries (GBs), respectively [34]. The stoichiometric/elemental composition of CSCTO-15 was analyzed by EDX from the same SEM micrograph.

Figure 2b shows the peaks of Ca, Sr, Cu, Ti and O and their respective band energies, suggesting it is consistent with the base composition, with no impurities. The wt% and at.% are summarized in Fig. 2c (inset).

3.2 Dielectric behavior

The temperature dependence of the relative dielectric constant and loss factor for CSCTO-15 at various frequencies is shown in Fig. 3. Here it is observed that both remain temperature-independent in the low-temperature region and then rapidly increase with increasing temperature (Table 2). Such a low value of dielectric constant in the low-temperature region indicates the absence of any significant dipolar interaction under the action of the applied electric field [22]. The rate of increase is greater at lower frequencies than at higher frequencies. Together, these observations indicate that the Maxwell–Wagner mechanism controls the polarization mechanism. However, the dielectric constant increases sharply in the high-temperature region. Furthermore, the trend in the increase of the dielectric constant in the high-temperature region decreases with the increase in applied frequency. A conducting grain with an insulating grain boundary produces

Table 1 Refinement coefficient (*Rwp*, *Rexp*, *Rp*, GoF and *R*-Bragg) of pure CCTO and Sr-doped CCTO

Sample name	R_p	R_{wp}	R_e	GoF	R-Bragg	Volume	Lattice parameter ($a=b=c$)
CCTO (X = 0.0)	17.86	21.85	16.83	1.6	2.90	402.105	7.395
CSCTO (X = 0.15)	28.5	16.7	8.99	1.7	2.94	403.204	7.403

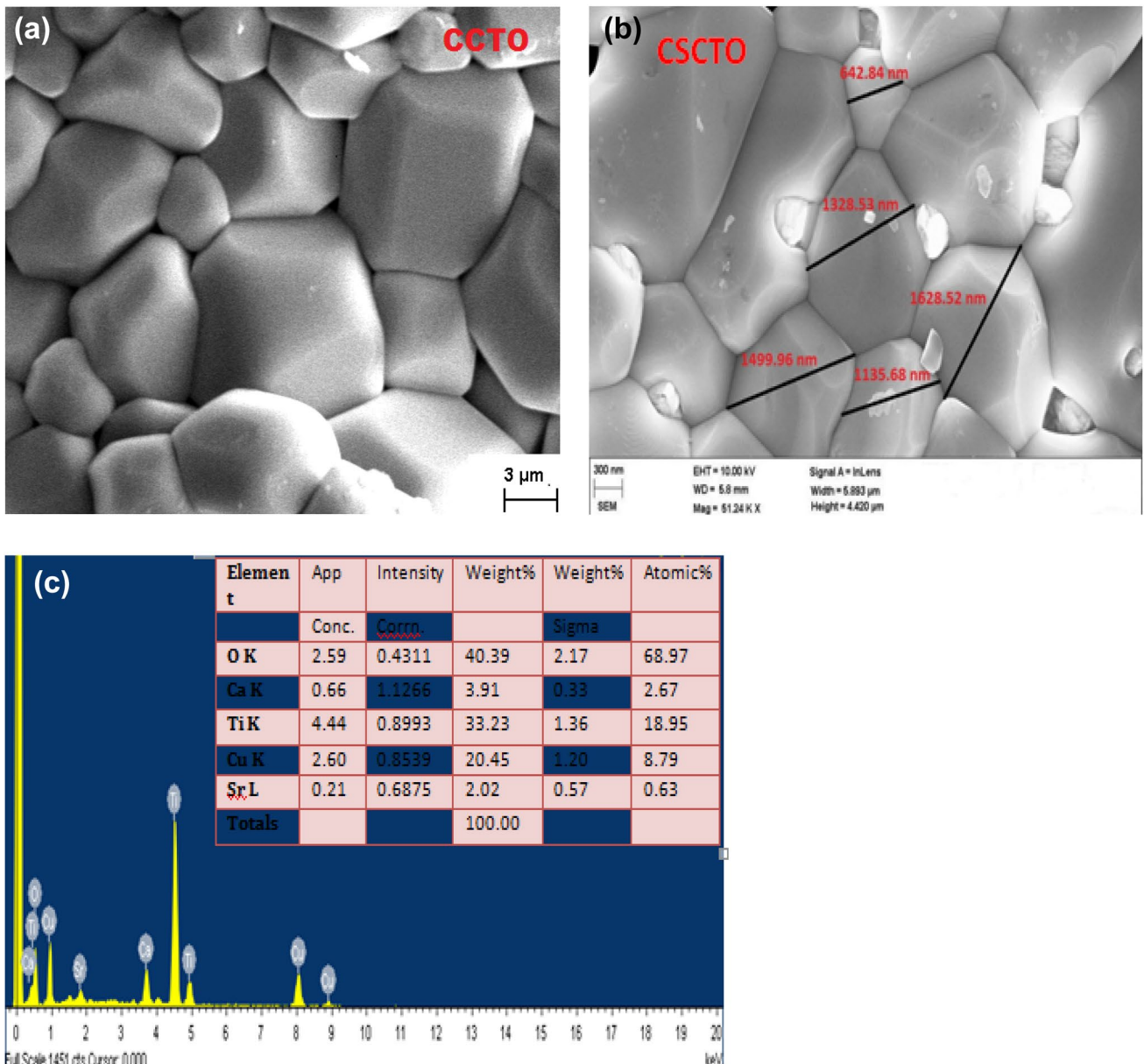| Element	App	Intensity	Weight%	Weight%	Atomic%
	Conc.	Corrn.		Sigma	
O K	2.59	0.4311	40.39	2.17	68.97
Ca K	0.66	1.1266	3.91	0.33	2.67
Ti K	4.44	0.8993	33.23	1.36	18.95
Cu K	2.60	0.8539	20.45	1.20	8.79
Sr L	0.21	0.6875	2.02	0.57	0.63
Totals			100.00		

Fig. 2 Surface micrographs of **a** CCTO and **b** CSCTO-15, and **c** EDX inset showing the at.% and wt% of CSCTO-15

an SBLC and IBLC, and also explains the high dielectric permittivity of the prepared sample. Similarly, a sharp increase in the dielectric loss in the high-temperature region may be attributed to the increased mobility of charge carriers due to defects or vacancies in the sample [23]. Also, the increased conductivity at elevated temperatures, thermally assisted electric charge carriers and relaxation process may cause the sharp increase in the tangent loss factor [16, 32]. Therefore, it is believed that said sample with high dielectric constant and low dissipation factor at higher temperatures is best suited for high-temperature applications, and also in devices such as transistors and microelectronic devices. [6, 37]. Both dielectric constant

and tangent loss are also high at lower frequency, but fall with rising frequency, as shown in Fig. 3. For CSCTO-15, the dielectric permittivity of 30,000 and loss factor of 2.4 is observed for 1 kHz at 300 °C. It indicates the presence of dipolar relaxation phenomena in our composition. Xue et al. reported a dielectric constant of 4×10^4 and loss of 0.5 for 10 wt% Sr-doped CCTO at 10 kHz and 120 °C.

A comprehensive effort has been made to understand the conduction mechanism in CSCTO-15 using different characterization techniques. One strategy for understanding the electrode performance is to understand the charge transport mechanism with respect to the temperature and frequency. The study of the frequency and temperature
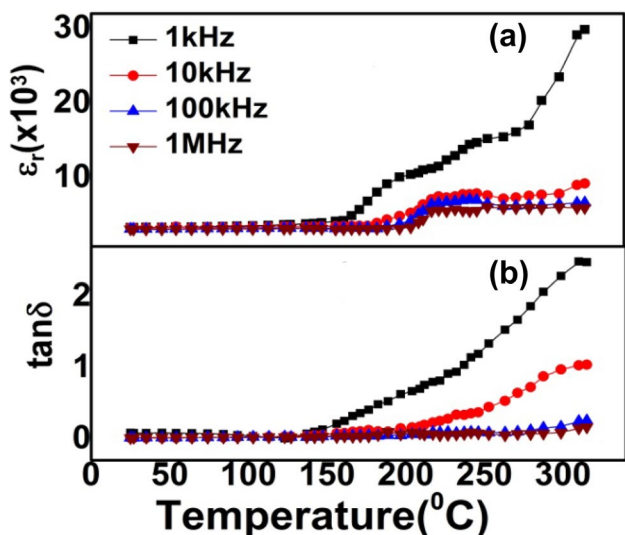
Fig. 3 Variation in **a** permittivity and **b** loss factor with temperature of CSCTO-15 at different frequencies

dependence of the dielectric constant may provide an opportunity to gain a better understanding of the details of electronic/ionic migration mechanisms [17].

3.3 Electrical conductivity studies

The conductance remains constant in the region of low frequency and rises on increasing the field for pure CCTO, as observed from frequency-dependent ac electrical conductivity [25]. Figure 4a illustrates the variation in ac electrical conductivity (σ_{ac}) of CSCTO-15 relative to the frequency of the supplied electric field at different temperatures. The ac electrical conductivity has been analyzed using the equation $\sigma_{ac} = 2\pi \tan\delta \, \varepsilon_r \, \varepsilon_o$. In this equation, dielectric data (i.e. ε_r, ε_o), $f =$ linear frequency of the ac field, and tan $\delta =$ tangent loss are used. From Fig. 4a, it is concluded that at all temperatures, conductivity strongly depends on the frequency. In the low-frequency domain, a plateau region is viewed in the compound. It indicates the existence of dc conductivity at low frequency.

These observations show the behavior of conductivity as a function of temperature and frequency. The Arrhenius plot for electrical conductivity of CSCTO-15 at different frequencies is merely shown in Fig. 4b. For the conduction process, the activation energy (E_A) can be considered from the slope of the line according to Arrhenius equation [26]:

$$\sigma = B \exp(-E_A/k_B T)$$

Table 2 Values of R_g (Ω), C_g, R_{gb} (Ω), C_{gb}, R_e and C_e of CSCTO-15

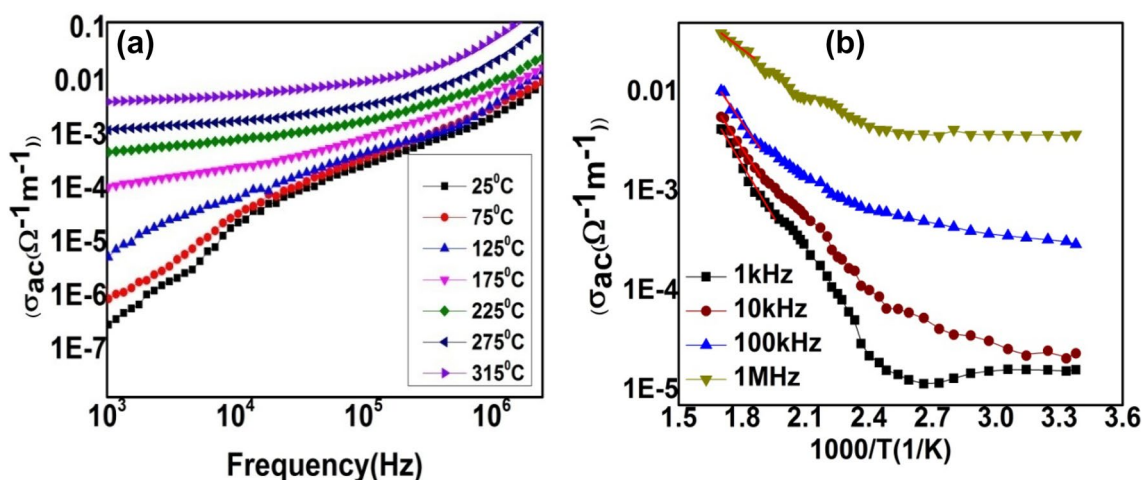| Temperature	R_g (Ω)	C_g	R_{gb} (Ω)	C_{gb}	R_e	C_e
25	4.819×10^5	2.274×10^{-10}	8.524×10^7	1.355×10^{-10}		
75	2.715×10^5	2.367×10^{-11}	7.840×10^7	1.381×10^{-10}		
125	1.618×10^4	1.508×10^{-9}	1.000×10^{15}	3.447×10^{-10}		
175	1.759×10^4	4.411×10^{-10}	2.098×10^6	6.568×10^{-10}		
225	1.143×10^5	2.465×10^{-10}	2.494×10^5	2.153×10^{-9}		
275	7.143×10^4	4.339×10^{-10}	1.000×10^{20}	7.680×10^{-9}	1.164×10^1	2.660×10^{-20}
325	9.994×10^4	1.000×10^{-20}	1.237×10^6	1.218×10^{-9}	3.738×10^3	1.031×10^{-9}

Fig. 4 **a**, **b** Variation in ac conductivity (σ_{ac}) of CSCTO-15 at different temperatures and frequencies

where E_A is the activation energy, k_B is the Boltzmann constant, B is the pre-exponential factor, and T is the absolute temperature. Using this expression, the calculated activation energy is found to be 0.7, 0.64, 0.6 and 0.31 eV at 10, 100, 500 kHz and 1 MHz frequency, respectively. In general, at high temperatures, the anion vacancies (holes) are more activated [18], since more activation energy is required for them than electrons. Hence, the value of conductivity is increased with a rise in temperature. Conduction in the high-temperature region is due to holes as well as electrons, whereas in the low-temperature region it is mainly due to electrons [18]. However, at low temperatures, the smaller activation energy may be attributed to the hopping process of electrons between ions of different valences [9]. Low electrical conductivity in the sample may be due to high grain boundary density [7]. The ferroelectric behavior of the prepared materials is linked to the conduction mechanisms. For the perovskite ferroelectrics, oxygen vacancies are one of the mobile charge carriers. In these systems, the Kröger–Vink notation is used to represent ionized oxygen vacancies that can be formed when the oxygen releases electrons [28]

$$O_0 = \frac{1}{2}O_2 + V_o' + e^- \tag{1}$$

$$O_0 = \frac{1}{2}O_2 + V_0'' + 2e^- \tag{2}$$

During this process, Ti^{4+} ions may capture these liberated electrons to form Ti^{3+} ions, and the electron hopping from Ti^{4+} to Ti^{3+} causes the overall electronic conductivity, which is both frequency- and temperature-dependent [13].

3.4 Impedance spectrum analysis

Impedance spectrum analysis is used to interpret the real (resistive) and imaginary (reactive) components of the complex impedance (Z^*) of the materials. In order to explain the electrical response of grains and GBs of sintered CSCTO-15 ceramic, a non-destructive technique such as impedance spectroscopy is used.

Generally, using the two quantities, (a) complex capacitive and (b) impedance, quantities of dielectric properties of materials can be described as a function of frequency.

Complex dielectric constant (ε^*), $\quad \varepsilon^* = \varepsilon' - j\varepsilon'' \tag{3}$

Complex impedance (Z^*), $\quad Z^* = Z' - jZ'' = R_s - \dfrac{j}{\omega c_s} \tag{4}$

Dielectric modulus (M^*), $\quad M^* = M' + jM'' = j\omega CoZ * \omega \tag{5}$

Dielectric loss ($\tan\delta$) $\tan\delta = \dfrac{\varepsilon''}{\varepsilon'} = \dfrac{-Z'}{Z''} = \dfrac{M''}{M'} \tag{6}$

The parameters ω, R_s and C_s are known as angular frequency, resistance and capacitance, respectively, in the above equations. Using Eqs. (1)–(4), there is a wide scope for graphical representation to estimate the contributions of the above parameters of the electrode/ceramic/electrode system. Figure 5a, b shows the variation in Z' (resistivity component) and Z'' (reactive component) as a function of frequency. Resistivity and reactive components are expressed as below.
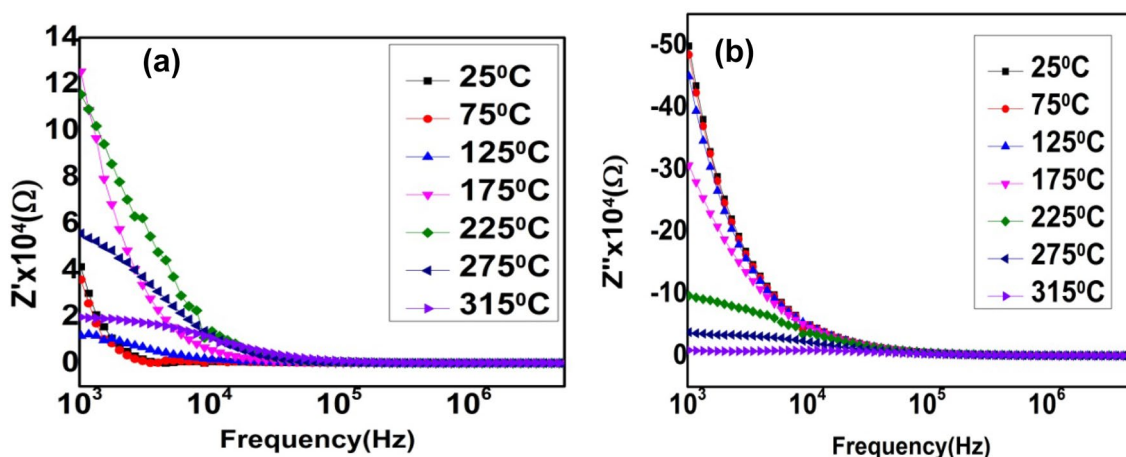
$$Z' = \frac{R}{1 + (\omega\tau)^2} \tag{7}$$

Fig. 5 Frequency dependence of **a** Z' and **b** Z'' of CSCTO-15 at selected temperatures

$$Z'' = \frac{\omega R\tau}{1 + (\omega\tau)^2} \qquad (8)$$

To a great extent, in the lower-frequency range, there is a reduction in the value of Z' with an increase in temperature, demonstrating NTCR (semiconducting) behavior. The Negative temperature cofficient resistance (NTCR) property is altered considerably in the high-frequency region, presenting complete fusion of Z' curves over a definite frequency. At higher frequencies, the magnitude of Z' for every temperature converges, indicating the possible release of space charge [11].

Figure 5b reveals that as the temperature increases, the loss peaks shift towards the higher-frequency region, and all Z'' curves converge at high frequencies (for all temperatures). This is a sign of the nature of bulk resistance, possible release of space charge at the grain boundaries and the presence of the dielectric relaxation process in the compound is expected [3]. The relaxation process may occur as a result of the existence of immobile/electron species at lower temperatures and defects/vacancies at high temperatures [27]. Also, the value of Z'' decreases steadily with a shift in the characteristic frequency towards the high-frequency side, and hence they ultimately converge in the higher-frequency side; due to the accumulation

of space charge [11]. Further, a large broadening of the peaks relative to temperature again indicates the occurrence of the temperature-dependent relaxation process in the material. The widths of the peaks suggest a spread of relaxation times.

3.5 Nyquist plot

The Nyquist plot of the pure CCTO showed the contribution of grain, grain boundary and electrode effects, and a non-Debye relaxation process was reported [25]. The Nyquist diagram (Fig. 6a, b) illustrates the relationship between the real and imaginary parts of the impedance at different temperatures and frequencies. It helps to identify the role of the electrode interface, grain boundary and grain effects associated with the polarization mechanism. It is observed that successive semicircle arcs are formed in the diagram which describe these three effects. Extension of the intercept of semicircles on the x-axis (real axis) and its number in the spectrum provide information regarding electrical processes occurring within the sample. The connection between these arcs and microstructure of the compound is recognized by sketching an equivalent electrical circuit. In polycrystalline specimens, grains are semiconducting, whereas the grain boundaries are insulating.
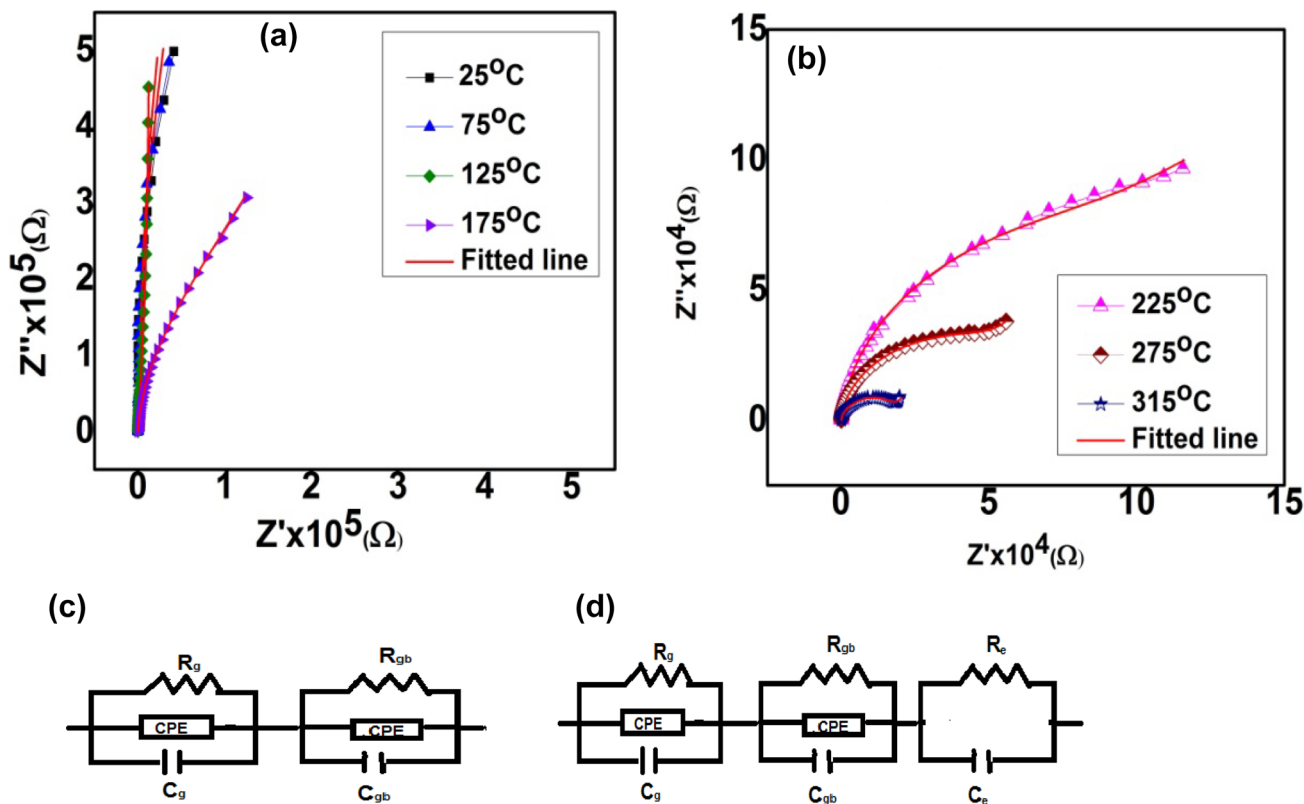

Fig. 6 **a**, **b** Nyquist plot of CSCTO-15 at different temperatures with **c**, **d** equivalent circuit diagrams

The semiconducting nature of the grains in ceramic samples is believed to be owing to the loss of oxygen during the high-temperature sintering route.

We can model an equivalent circuit (Fig. 6d, f) to describe a physical mechanism occurring in the sample with the help of impedance spectra. A computer-controlled software package (ZSimpWin version 2.0) is used to fit the theoretically calculated data with experimental data to determine the type of the relaxation mechanism (Debye or non-Debye). The simulated circuit consists of a parallel arrangement of bulk capacitance (C_g) and resistance (R_b), with grain boundary capacitance (C_{gb}), which corresponds to the constant phase element (CPE = Q) coefficient and grain boundary resistance (R_{gb}) connected in a series arrangement. The nature of the material (experimental and theoretical fit plot) was analyzed using software and is summarized in Table 1. Due to inhomogeneous distribution of grains, depressed semicircles or arcs will be observed in impedance spectroscopy plots; to fit the ideal capacitor to the data is not possible. The ideal capacitor is used only when exact semicircles are formed, in the case of homogeneous distribution of grains and when grain growth takes place; however, in practice, it is not possible to obtain exact semicircles. Thus, by using the CPE, it is possible to extract C values. The phase angle of the CPE impedance has a value of $-(90*n)°$. For $n = 1$, it behaves like a capacitor. For $n = 0$, it behaves like a resistor, and for $n = -1$, like an inductor. The Kröger–Vink notation was used by Cortes et al. to understand the dielectric and non-ohmic properties of low-Sn^{4+}-substituted samples ($x = 0.1$ and $x = 0.2$) into a CCTO/CTO composite [4].

4 Conclusion

In summary, the hopping type of conduction and dielectric phenomena have been systematically investigated for CSCTO-15 sample. The prepared sample crystallizes in a cubic crystal system, which was confirmed from the structural refinement of X-ray diffraction data. The surface morphology shows grain (various sizes) and clear grain boundaries suggesting a highly densified ceramic sample. The Maxwell–Wagner model and interfacial polarization explains the higher dielectric constant of the material at higher temperatures. As the tangent loss was low and the Q factor (quality factor) of the compound very high, the material can be used for various applications, including microwave laminates and appliances. The conductivity vs. temperature graph, confirms that in the low-temperature region, the conductivity of CSCTO-15 is relatively low. This may be due to high grain boundary density, which results in increased grain boundary resistance. The graphs of complex impedance show that the

sample reveals semiconducting behavior and the relaxation phenomenon.

Compliance with ethical standards

References

1. Adams TB, Sinclair DC, West AR (2002) Giant barrier layer capacitance effects in CaCu3Ti4O12 ceramics. Adv Mater 14:1321–1323. https://doi.org/10.1002/1521-4095

2. Boonlakhorn J, Kidkhunthod P, Thongbai P (2017) Significantly improved non-Ohmic and giant dielectric properties of CaCu3-xZnxTi4O12 ceramics by enhancing grain boundary response. Ceram Int 43:2705–2711. https://doi.org/10.1016/j.ceramint.2016.11.089

3. Behera B, Nayak P, Choudhary RNP (2007) Impedance spectroscopy study of NaBa2V5O15 ceramic. J Alloy Compd 436:226–232. https://doi.org/10.1016/j.jallcom.2006.07.028

4. Cortés JA, Cotrim G, Orrego S, Simões AZ, Ramírez MA (2018) Dielectric and non-ohmic properties of Ca2Cu2Ti4-xSnxO12 (0.0 ≤ x ≤ 4.0) multiphasic ceramic composites. J Alloy Compd 735:140–149. https://doi.org/10.1016/j.jallcom.2017.11.089

5. Deng J, Liu L, Sun X, Liu S, Yan T, Fang L, Elouadi B (2017) Dielectric relaxation behavior and mechanism of Y2/3Cu3Ti4O12 ceramic. Mater Res Bull 88:320–329. https://doi.org/10.1016/j.materresbull.2017.01.005

6. Damjanovic D (1998) Materials for high temperature piezoelectric transducers. Curr Opin Solid State Mater Sci 3:469–473. https://doi.org/10.1016/S1359-0286(98)80009-0

7. Duran P, Tartaj J, Capel F, Moure C (2003) Processing and characterisation of a fine nickel oxide/zirconia/composite prepared by polymeric complex solution synthesis. J Eur Ceram Soc 23:2125–2133. https://doi.org/10.1016/S0955-2219(03)00028-1

8. Fang TT, Liu CP (2005) Evidence of the internal domains for inducing the anomalously high dielectric constant of CaCu3Ti4O12. Chem Mater 17:5167–5171. https://doi.org/10.1021/cm051180k

9. Gabal MA, Abdel-Daiem AM, Al Angari YM, Ismail IM (2013) Influence of Al-substitution on structural, electrical and magnetic properties of Mn–Zn ferrites nanopowders prepared via the sol–gel auto-combustion method. Polyhedron 57:105–111. https://doi.org/10.1016/j.poly.2013.04.027

10. Hu Y, Jeng TS, Liu JS (2012) Effect of the MgO substitution for CuO on the properties of CaCu3Ti4O12 ceramics. Ceram Int 38:3459–3464. https://doi.org/10.1016/j.ceramint.2011.12.059

11. Jonscher AK (1977) The 'universal' dielectric response. Nature 267:673–679. https://doi.org/10.1038/267673a0

12. Jansen E, Schäfer W, Will G (1994) R values in analysis of powder diffraction data using Rietveld refinement. J Appl Cryst 27:492–496. https://doi.org/10.1107/s0021889893012348

13. Kumar N, Ghosh A, Choudhary RNP (2011) Electrical behavior of Pb(Zr0.52Ti0.48)0.5(Fe0.5Nb0.5)0.5O3 ceramics. Mater

Chem Phys 30:381–386. https://doi.org/10.1016/j.matchemphys.2011.06.059

14. Liu G, Fan H, Xu J, Liu Z, Zhao Y (2016) Colossal permittivity and impedance analysis of niobium and aluminum co-doped TiO2 ceramics. RSC Adv 6:48708–48714. https://doi.org/10.1039/C6RA07746C

15. Li T, Liu D, Dai H, Xing H, He H, Chen Z (2014) Effect of defect on the nonlinear and dielectric property of Ca(1−x)SrxCu3Ti4O12 ceramics synthesized by sol–gel process. J Alloy Compd 599:145–149. https://doi.org/10.1016/j.jallcom.2014.02.076

16. Mahamoud H, Louati B, Hlel F, Guidara K (2011) Impedance and modulus analysis of the (Na0.6Ag0.4)2PbP2O7 compound. J Alloy Compd 509:6083–6089. https://doi.org/10.1016/j.jallcom.2011.03.027

17. Martines RF, Brant MC, Domingues RZ, Paniago RM, Sapag K (2009) Synthesis and characterization of NiO-YSZ for SOFCs. Mater Res Bull 44:451–456. https://doi.org/10.1016/j.materresbull.2008.04.017

18. Manikandan M, Venkateswaran C (2014) Effect of high energy milling on the synthesis temperature, magnetic and electrical properties of barium hexagonal ferrite. J Magn Magn Mater 358–359:82–86. https://doi.org/10.1016/j.jmmm.2014.01.041

19. Nachaithong T, Tuichaic W, Kidkhunthodd P, Chanlekd N, Thongbaib P, Maensiri S (2017) Preparation, characterization, and giant dielectric permittivity of (Y3+ and Nb5+) co–doped TiO2 ceramics. J Eur Ceram Soc 37:3521–3526. https://doi.org/10.1016/j.jeurceramsoc.2017.04.040

20. Ni L, Chen XM (2007) Dielectric relaxations and formation mechanism of giant dielectric constant step in CaCu3Ti4O12 ceramics. Appl Phys Lett 91:122905. https://doi.org/10.1063/1.2785128

21. Prompa K, Swatsitang E, Saiyasombat C, Putjuso T (2018) Very high performance dielectric and non-Ohmics properties of CaCu3Ti4.2O12 ceramics for X8R capacitors. Ceram Int 44:13267–13277. https://doi.org/10.1016/j.ceramint.2018.04.156

22. Pandey N, Thakur AK, Choudhary RNP (2008) Studies on dielectric behaviour of an oxygen ion conducting ceramic—CaMnO3-δ. Indian J Eng Mater Sci 15:191–195

23. Pattanayak S, Priyadarshan A, Subudhi R, Nayak RK, Padhee R (2013) Tailoring of electrical properties of BiFeO3 by praseodymium. J Adv Ceram 2:235–241. https://doi.org/10.1007/s40145-013-0065-x

24. Subramanian MA, Dong Li, Duan N, Reisner BA, Sleight AW (2000) High dielectric constant in ACu3Ti4O12 and ACu3Ti3FeO12 phases. J Solid State Chem 151:323–325. https://doi.org/10.1006/jssc.2000.8703

25. Sahu M, Choudhary RNP, Das S, Otta S, Roul BK (2017) Intergrain mediated intrinsic and extrinsic barrier layer network mechanism involved in Ca1Cu3Ti4O12 bulk ceramic. J Mater Sci Mater Electron 28:15676–15684. https://doi.org/10.1007/s10854-017-7457-6

26. Sudha LK, Roy S, Uma Rao K (2014) Evaluation of activation energy (Ea) profiles of nanostructured alumina polycarbonate composite insulation materials. Int J Mater Mech Manuf 2:96–100. https://doi.org/10.7763/IJMMM.2014.V2.108

27. Suman CK, Prasad K, Choudhary RNP (2006) Complex impedance studies on tungsten-bronze electroceramic: Pb2Bi3LaTi5O18. J Mater Sci 41:369–375. https://doi.org/10.1007/s10853-005-2620-5

28. Sen S, Choudhary RNP, Tarafdar A, Pramanik P (2006) Impedance spectroscopy study of strontium modified lead zirconate titanate ceramics. J Appl Phys 99:124114–124118. https://doi.org/10.1063/1.2206850

29. Schmidt R, Sinclair DC (2010) Anomalous increase of dielectric permittivity in Sr-doped CCTO ceramics Ca1-xSrxCu3Ti4O12. Chem Mater 22:6–8. https://doi.org/10.1021/cm903220z

30. Thongbai P, Jumpatam J, Yamwong T, Maensiri S (2012) Effects of Ta5+ doping on microstructure evolution, dielectric properties and electrical response in CaCu3Ti4O12 ceramics. J Eur Soc 32:2423–2430. https://doi.org/10.1016/j.jeurceramsoc.2012.02.048

31. Vangchangyia S, Yamwong T, Swatsitang E, Prasit Thongbai, Santi Maensirie (2013) Selectivity of doping ions to effectively improve dielectric and non-ohmic properties of CaCu3Ti4O12 ceramics. Ceram Int 39:8133–8139. https://doi.org/10.1016/j.ceramint.2013.03.086

32. Wang T, Jin L, Li C, Hu Q, Wei X (2015) Relaxor ferroelectric BaTiO3–Bi(Mg2/3Nb1/3)O3 ceramics for energy storage application. J Am Ceram Soc 98:559–566. https://doi.org/10.1111/jace.13325

33. Xue H, Guan X, Yu R, Xiong Z (2009) Dielectric properties and current–voltage nonlinear behavior of Ca1−xSrxCu3Ti4O12 ceramics. J Alloy Compd 482:L14–L17. https://doi.org/10.1016/j.jallcom.2009.03.190

34. Xue R, Zhao G, Chen J, Chen Z, Liu D (2016) Effect of doping ions on the structural defect and the electrical behavior of CaCu3Ti4O12 ceramics. Mater Res Bull 76:124–132. https://doi.org/10.1016/j.materresbull.2015.12.020

35. Zheng JC, Frenkel AI, Wu L, Hanson J, Ku W, Bozin ES, Zhu Y (2010) Nanoscale disorder and local electronic properties of CaCu3Ti4O12: an integrated study of electron, neutron, and x-ray diffraction, x-ray absorption fine structure, and first-principles calculations. Phys Rev B 81:144203. https://doi.org/10.1103/PhysRevB.81.144203

36. Zhang JL, Zheng P, Wang CL, Zhao ML, Li JC, Wang JF (2005) Dielectric dispersion of CaCu3Ti4O12 ceramics at high temperatures. Appl Phys Lett 87:142901. https://doi.org/10.1063/1.2077864

37. Zhang S, Yu F (2011) Piezoelectric materials for high temperature sensors. J Am Ceram Soc 94:3153–3170. https://doi.org/10.1111/j.1551-2916.2011.04792.x